

ARTICLE

Bringing ultimate depth to scanning tunnelling microscopy: deep subsurface vision of buried nano-objects in metals

Received 01th March 2022,
Accepted 00th Month 20xx

DOI: 10.1039/x0xx00000x

Oleg Kurnosikov*^{a, b}, Emilie Gaudry^a, Muriel Sicot^a, Danielle Pierre^a, Yuan Lu^a, Stéphane Mangin^a

Abstract

A method for subsurface visualization and characterization of hidden subsurface nano-structures based on Scanning Tunneling Microscopy/Spectroscopy (STM/STS) has been developed. The nano-objects buried under a metal surface up to several tens of nanometers can be visualized through the metal surface and characterized with STM without destroying the sample. This non-destructive method exploits quantum well (QW) states formed by partial electron confinement between the surface and buried nano-objects. The specificity of STM allows for nano-objects to be singled out and easily accessed. Their burial depth can be determined by analysing the oscillatory behaviour of the electron density at the surface of the sample, while the spatial distribution of electron density can give additional information about their size and shape. The proof of concept was demonstrated with different materials such as Cu, Fe, W in which the nanoclusters of Ar, H, Fe and Co were buried. For each material, the maximal depth of subsurface visualisation is determined by the material parameters and ranges from several nanometers to several tens of nanometers. To demonstrate the ultimate depth of subsurface STM-vision as the principal limit of our approach, the system of Ar nanoclusters embedded into a single-crystalline Cu(110) matrix has been chosen since it represents the best combination of the mean free path, smooth interface and inner electron focusing. With this system we experimentally demonstrated that Ar nanoclusters of several nanometers large buried as deep as 80 nm can still be detected, characterized and imaged. The ultimate depth of this ability is estimated as 110 nm. This approach using QW states paves the way for an enhanced 3D characterization of nanostructures hidden well below a metallic surface.

New concept

It is of common belief that STM/STS is a characterization method applied exclusively to a surface or objects on it. However, some reports show that subsurface single atomic impurities or shallow nanostructures could be recognized with STM as well. The presence of such objects in close proximity to the surface would induce a tiny surface deformation or a perturbation of the local density of electronic states (LDOS) at the surface, which can actually be detected with STM/STS. The embedded objects, detected by a local change in surface properties, are reported to be no more than a couple of nanometres below the surface. So far, the question of how deep an STM can in principle detect the hidden objects below a surface has never been considered. The actual study demonstrates the depth record of about one hundred of nanometers achieved at visualization of subsurface nanoclusters in a metallic sample with STM. To get this extremely deep STM-vision, we exploit QW states formed by delocalized electron states confined between the surface of the metal and the local interface with the nanoclusters. Additionally, we profit from electron focusing of bulk electronic states due to an appropriate band structure of the metal. The spatial variation and the oscillations of conductance spectra measured by STS at the surface allows to determine the location, depth, and size of the buried nanoclusters, as well as to indicate their shape. The ultimate subsurface STM-vision has been realized and analyzed in detail using Ar nanoclusters embedded in the Cu(110) matrix providing a record depth value. With other systems, such as Ar, H, Fe, Co nanoclusters in Fe, W, and Cu matrices we confirmed the versatility of our method. Our approach paves the way for non-destructive STM characterization of buried nanostructures and triggers the development of 3D subsurface nano-analysis with STM.

Introduction

Scanning tunnelling microscopy (STM) and spectroscopy (STS) have become a widely used technique for imaging surface structures with atomic resolution [1] and determining the local

^a Université de Lorraine, Institut Jean Lamour, France.

^b ex. Technische Universiteit Eindhoven, department of Applied Physics, Netherlands.

* Contact address: Oleg.Kurnosikov@univ-lorraine.fr

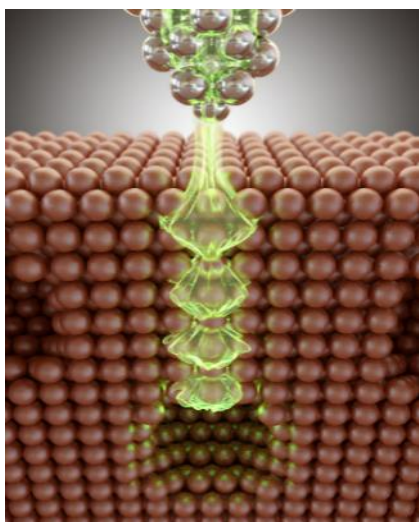


Fig. 1 Illustration of the concept of subsurface STM vision based on the near-surface resonances of non-localized electronic states of the matrix material.

density of electronic states (LDOS) of surface atoms, molecules or nanostructures [2]. The extremely high surface sensitivity of this technique is a direct consequence of a strong exponential decay of the probability of tunnelling selecting the atoms closest to the tip. Therefore, it is commonly believed that an STM can be used exclusively for characterization of a surface as well as atomic, molecular and nanostructures on it. For profiling structures below a surface, the STM still can be used together with sample-destructive post-processing like milling [3] or cleaving the sample [4]. This destructive post-processing forms a new surface from deeper layers of materials or in cross-sections and then STM performs the surface characterization on them. This way for accessing deeper structures is widely used also for depth profiling study with transmission electron microscopy [5], scanning electron microscopy [6], as well with electron spectroscopy [7]. However, this sample-destructive technique has drawbacks as the interfaces an embedded structures can be damaged during the sample post-processing. Frequently, the destructive post-processing has to be performed in several stages or with a set of the samples for detailed characterization.

In this article, we develop the subsurface STM/STS vision through a metallic surface for characterisation of the nano-objects buried up to 100 nm below the surface excluding any sample-destructive post-processing like milling or cleaving. Our approach allows to see nano-objects at different depths with one STM scan and to determine their locations and depths for a wide variety of conductive materials of substrates. In addition, the size of the subsurface nanostructures can be determined or estimated if the electronic structure of the substrate is suitable and known. In this case, the spatial distribution of scanned anomalies can even provide more insight into the shape of buried nanostructures. Avoiding any sample-destructive post-processing gives an opportunity to follow the evolution of the

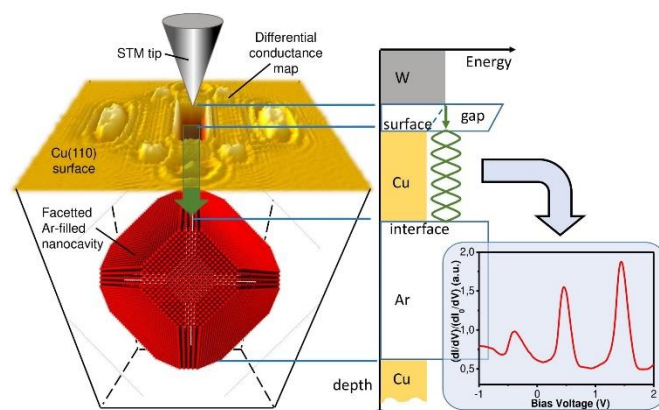


Fig. 2. Schematic drawing of realisation of the subsurface detection of hidden nanocluster. Left panel illustrates the configuration of the system and lateral distribution of the surface conductance induced by the subsurface nanocluster with a faceted interface. The middle panel is the corresponding energy diagram leading to the measured oscillatory behaviour of the normalized differential conductance in STS spectrum displayed in the bottom right panel.

systems with embedded nano-objects in time under different activation processes.

The ability of the STM to indicate in its images the presence of subsurface objects was demonstrated previously, but it was not widely used for subsurface characterisation. There are some examples of STM images showing that tiny deformations of the surface or an appearance of additional electronic states at the surface can be attributed to subsurface atoms or nanostructures buried [8, 9, 10] one or a couple atomic layers below a surface. In semiconductors, near-surface impurities are recognized as extra features superimposed onto the STM images of a surface [4, 11–14]. Such effects can become very spectacular in the case of single dopants in semiconductors since the embedded charges and states of the dopants are not screened over the distance of several nanometers and therefore contribute directly to the LDOS at the surface [15].

As a contrary, in materials with a very high electron density like metals, such subsurface impurities and defects buried several nanometers underneath can not be detected as easily since their states and charges are screened already over the interatomic distances. As a consequence, subsurface STM vision at the depth on the nanometre scale in metals is considered to be unrealistic.

In this article, we oppose this statement by presenting an experimental evidence of the extremely deep subsurface vision in metals with STM. Instead of direct detection of the localized electronic states belonging to the buried impurities or nanostructures we use bulk non-localized states of the host material (Fig. 1). The electron density of the bulk between the surface and the buried nano-object gets the oscillating component and this component can be probed with STS at the surface near the location of the hidden nanoobject. Because the

length of delocalization of these states can be very large, a deep subsurface structure can be detected.

Previously, several STM experiments reported the use of LDOS oscillations in a metallic layer for the subsurface detection and thus confirm the validity of this approach. For example, the steps at Si substrate covered with a flat Pb layer were imaged by analysing LDOS variation on the flat surface of lead [16-23] whereas the same effect was also observed with thin films of Cd [24]. A similar concept has been used by Weissman *et al.* [25] and Kotzot *et al.* [26]. They were able to locate subsurface impurity atoms buried several atomic layers below the Cu surface by treating the diameter of oscillating LDOS rings. The spatial oscillations of LDOS induced by electron scattering at a subsurface atom is theoretically described by Avotina *et al.* [27] and Lunis *et al.* [28]. There are also a few examples of imaging the subsurface nanoobjects showing stronger signal due to efficient reflection. The systems are represented by nanocavities formed in metals like Cu, Pb, Ag or Al and filled in by noble gases [29-36]. However, the typical depth of location of subsurface structures in these reports does not exceed a couple of nanometers while the signals still reveal remarkable and measurable oscillations in LDOS. This indicates that the limit in the depth has not been achieved.

In this article, we show that the limit of subsurface vision can be pushed in one or two orders more than previously reported. For illustration, we exploited an ideal system which was used in pioneering works of Adam *et al.* and Kurnosikov *et al.* [33-35], however they reported only some particular results. Understanding of all limiting factors allowed us to achieve the depth of subsurface vision in our experiments up to to 80 nm and estimate the ultimate depth of detection of around 110 nm.

Principles

As well known, the LDOS could be accessed by means of STS at the surface [2]. The LDOS at the surface is usually determined by the band structure of material at corresponding crystallographic orientation, by the states associated with the crystal termination, so-called surface states, and by localized states of single atoms or molecules in- and on the surface. The last type of states is mostly used for the visualization of atomic structure in STM images, whereas the two first ones usually contribute to a homogeneous background, which meets much less of interest in STM applications. However, in some cases the delocalized states can reveal interesting features in the STM/STS images. Regarding a system with *surface delocalized* states, for example the stepped surface of Cu(111) or the same surface with surface impurities, standing wave patterns of electron density can be observed on STS maps [37]. The standing waves surround the impurity atoms or group near the step edges since they originate from the scattering of delocalized surface electrons on these objects and electron wave interference. Exactly the same mechanism of formation of standing wave of electron density should be realized also in volume for *bulk delocalized* electronic states in case of the scattering or reflection from the objects located in the bulk, *i.e.* below the surface. In this case, however, the deep subsurface object cannot be reached with the STM probe and therefore

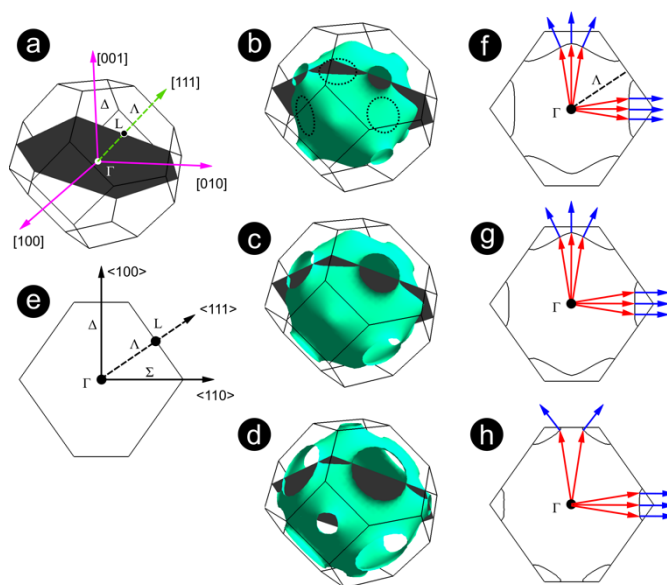


Fig.3 Principles of electron focusing in Cu: (a) First Brillouin zone (BZ) of an *fcc* lattice with relevant high-symmetry *k*-points, directions and lattice vectors. The grey plane is $[1/2, 1/2, 1]$; (b-d) Iso-energetic surfaces obtained from the calculated band structure of Cu in reciprocal space at (b) Fermi level, E_F (Fermi surface), (c) $E_F + 1$ eV and (d) $E_F + 2$ eV. The encircled areas in (b) highlight the saddle zones close to the $\langle 110 \rangle$ directions that are locally almost flat. (e) Cross-section between the grey plane and the first BZ in (a); (f-h) Cross-sections related to the grey plane $[1/2, 1/2, 1]$ in (a, e) at the corresponding energies (f) E_F , (g) $E_F + 1$ eV, and (h) $E_F + 2$ eV, respectively. Red arrows illustrate *k*-vectors in the $\langle 110 \rangle$, $\langle 100 \rangle$, and close to them directions. Blue arrows indicate the directions of the group velocity. The propagation of electron waves with *k*-vectors around the $\langle 110 \rangle$ are almost parallel, whereas it diverges for electron packages with *k*-vectors close to the $\langle 100 \rangle$.

does not appear in STM images. Nevertheless, the perturbation of the spectra of delocalized bulk states due to subsurface scattering can be observed *at the surface* as well. The perturbation of the spectra appears as superimposed electron density oscillations across the surface as well as the oscillation of electron density probed in a selected location versus energy since the electrons at the scattering obey a wave equation. Considering the scattering from a bigger subsurface object, like an interface with some buried nanocluster and a free flat surface, one can expect a multiple electron reflections between them. In this case, the interface and surface serve as boundaries partially confining the delocalised bulk electrons. The partial confinement could lead to a formation of localized near-surface quantum well (QW) resulting in much stronger quasi-periodical variation of the electron density. A schematic representation of such a geometry and its corresponding energy landscape is given in Fig.2. Therefore, the observation of *oscillatory component* in LDOS revealed by STS above the buried nanostructure can be used for the detection of buried nanoparticle. Moreover, by analysing the period of oscillation

ΔV , it would also be possible to determine depth d of confinement of the bulk states that is also the depth of the corresponding facet of the subsurface structure, using the following formula:

$$d = \pi(dE/dk) \cdot 1/(e\Delta V) \quad (1)$$

where dE/dk is derivative of energy E by the wave vector of electrons k in the appropriate direction deduced from the band structure and e is the electron charge. Beside the depth of location, also the shape or size of the subsurface structure can be reconstructed considering the lateral variation of LDOS with a corresponding model [33–34].

Thus, the ability to detect and characterize the subsurface nanoclusters is based on the presence of the oscillatory component of LDOS in STS signal. The amplitude of this component and its oscillation period decrease with d increase. Therefore, an ultimate depth of detection would be defined as the depth when the oscillations are no longer recognizable in STS measurements.

Several factors are responsible for the formation of oscillations and thus determining the ultimate depth of STM vision, namely the electronic coherence length, interface roughness, and the electronic band structure of the host material, as discussed below.

First, since the subsurface vision is based on the electron interference, the oscillation whose period is used to determine the depth d as expressed in formula 1 can occur if the depth does not exceeds the coherence length of the corresponding states. This coherence length is known to vary with the electronic mean free path (MFP). This last parameter, which is material-dependent, is limited by electron scattering on phonons, impurities or due to other collective interactions. Therefore, it varies with temperature T , impurities concentration, and electron energy. Overall, the MFP ranges from a few nanometers to several tenth of nanometers [38, 39]. Temperature modifies MFP such that MFP gets even much longer with T decrease. It is also noteworthy that temperature affects the broadening of the LDOS oscillation peaks belonging to each QW resonances. As a consequence, T will have an influence on the ultimate depth detection.

Second, the coherence can also be partially or completely lost at the reflection due to a rough interface. Therefore, buried nanostructures forming atomically flat interfaces with the host material are more likely to be detected with STM.

Third, the electronic band structure of the host material is important as well in determining the ultimate depth of detection. Its angular distribution is responsible for the divergence and decay of the electronic state packages since an STM probes the states with some variety of k -vectors in the three-dimensional reciprocal space. The decay depends on the direction of electron wave packages propagation in the bulk. As well known, the direction of propagation of wave package in the bulk at low energy is determined by the vector of group velocity $\mathbf{v}_g(\mathbf{k})$:

$$\mathbf{v}_g(\mathbf{k}) = \nabla_{\mathbf{k}} E(\mathbf{k}) \quad (2)$$

where the electronic dispersion relations $E(\mathbf{k})$ can be determined theoretically or experimentally in the form of electronic band structures [40]. According to formula (2), at a specific energy E_0 that can be experimentally set with STM choosing a bias voltage V_0 such that $E_0 = eV_0$, in reciprocal space, the group velocity \mathbf{v}_g is perpendicular to the iso-energetic surface of the host material. In case the bias is set to zero, the energy dispersion surface corresponds to the Fermi surface. In previous works [27, 28, 41, 42], it has been shown that the contours of the Fermi surface affect the direction of the group velocity. Specifically, when injecting electrons into directions where the Fermi surface is almost flat, the group velocity stays parallel for some close range of \mathbf{k} . This effect has been called the focusing effect. On the contrary, where the Fermi surface has a more spherical shape, the group velocity tends to diverge and as a consequence, the propagation directions are more spread. This has been illustrated experimentally in the case of single Co atoms embedded into a Cu(111) single crystal and theoretically explained using the Fermi surface of Cu [25, 28]. However, as the period of LDOS oscillations versus bias voltage is needed to determine the depth at which the object is buried, it is of paramount importance to not only consider the Fermi surface but contours at all energies within the range of the measure typically corresponding up to 2eV for a regular STS spectrum. Therefore, we have calculated iso-energy surfaces for Cu in the First Brillouin Zone shown in Fig.3(a) setting the energy to the Fermi level E_F , $E_F + 1\text{eV}$, $E_F + 2\text{eV}$ as displayed in Fig. 3(b–d), respectively. In good agreement, with previous studies [25, 27, 28], the Fermi surface of Cu bear very flat regions with strongly suppressed curvature in $\langle 110 \rangle$ directions whereas necks resulting from band gap opening are observed in $\langle 111 \rangle$ directions around L points. In addition, energy bumps can be found in $\langle 100 \rangle$ directions around X points. Those three features remain valid within the range of 0–2eV as displayed in Fig. 3(b–d), respectively though the flat areas around Σ shrink with increasing energy due to the larger opening of the band gaps at L points. In order to better understand the influence of such contours on the focusing effect, we now discuss the anisotropy of the propagation of electronic waves in the STM experiment by looking at the group velocity as a function of the energy. To do so, we have chosen to consider a cross section between the plane $[\frac{1}{2} \frac{1}{2} 1]$ which contains the main 3 high-symmetry directions (see grey plane in Fig. 3(a) and its planar presentation in Fig. 3(e)) and the constant energy surfaces of Fig.3(b–d). The resulting cross-sections are displayed in Fig. 3(f–h) where red arrows illustrate \mathbf{k} -vectors whereas blue arrows indicate the group velocity giving the indication of the propagation direction, which is perpendicular to the contour displayed as black solid line. Obviously, upon increasing energy (*i.e.* bias voltage in STM experiment), the group velocity \mathbf{v}_g remains parallel to the $\langle 110 \rangle$ direction for the \mathbf{k} -vectors grouping around $\langle 110 \rangle$. However, if the corresponding \mathbf{k} -vectors lie around the $\langle 100 \rangle$ direction, the divergence of \mathbf{v}_g occurs due to the presence of an energy bump in the reciprocal space. This translates into the fact that if electrons are injected into a (110)-cut surface, they will propagate mostly following that direction

keeping the same amplitude over a long distance. However, their injection into the (001)-cut surface will result in a stronger decay due to the spatial divergence of corresponding propagating states. This discussion could be generalized to any other materials: flatness of the contour of iso-energetic surface would lead to a focusing effect of the injected electrons [41, 42].

Since the local flatness of the iso-energetic surface of copper in $\langle 110 \rangle$ allows to concentrate the electronic states in this direction, the oscillating STS signal should be more pronounced and it would be worth to use this direction for enhancing the ultimate depth of the subsurface electron vision.

Experiment

To demonstrate the subsurface STM-vision as well to illustrate its ultimate depth, we used several matrix materials such as Fe, W, and Cu with two different types of embedded nanoclusters, namely the insulating clusters of Ar and H, and the conductive nanoclusters of Co and Fe. Moreover, the systems of Fe/MgO and Bi/Fe were used to confirm that the same approach can be used in the characterization of buried interfaces (Supplementary materials). The non-conductive nanoclusters represent the ideal case of total reflection at the interface with the matrix material. Since the atomic electronic structure of Ar and H does not play any remarkable role in the electronic processes we consider, we can reasonably treat these nanoclusters in metals also as nanocavities with Ar or H filling. On the contrary, Fe and Co nanoclusters buried in Cu provide only partial electron reflection since the nanoclusters are conductive. However, the mismatch of k -vectors in Cu and Co or Fe yields the reflection sufficient to realise the subsurface vision with this kind of non-ideal system. The band structure of all these materials is well-determined and sample preparation is straightforward.

The Ar nanoclusters in copper and iron are formed by irradiating the Cu(110), Cu(001) and Fe(001) surfaces with a dose of $2 \cdot 10^{17} \text{ cm}^{-2}$ of Ar^+ ions with a kinetic energy of 5 keV and 1 keV, respectively. This ion energy was specifically chosen since it leads to a penetration of Ar into Cu up to 10 nm and a little bit less in Fe. In order to recover an atomically flat surface of Cu after irradiation with Ar, a moderate annealing at 1050K for 5 min was performed whereas Fe was annealed at 700K for 20 min. During this post-annealing, Ar segregation occurs. As a consequence, a significant part of the implanted Ar atoms reaches the surface and leaves the sample. However, some amount of the embedded Ar remains in the substrate forming nanoclusters of a typical size of around 2 - 10 nm. The processes of formation of the nanoclusters has been proved by XPS analysis [34, 36]. Additionally, the XPS spectra at the nanoclusters formation can be found in supplementary materials. Formation of H nanoclusters is performed in a similar way by irradiating the W(111) surface with H^+ ions with a kinetic energy of 0.7 keV. Consequent annealing at c.a. 2000K has been performed in the flash mode. To form Co and Fe nanoclusters embedded in Cu, a half of monolayer of Co or Fe was deposited on clean surfaces of the Cu(001), Cu(111) or Cu(110) crystals. The annealing at 550K led to formation of small nanoislands

embedded into the first two layers of copper [9]. Then they were buried further by extra deposition of Cu. Similarly, as we needed Ar nanoclusters buried deeper than those obtained after the implantation and the first thermal treatment, we

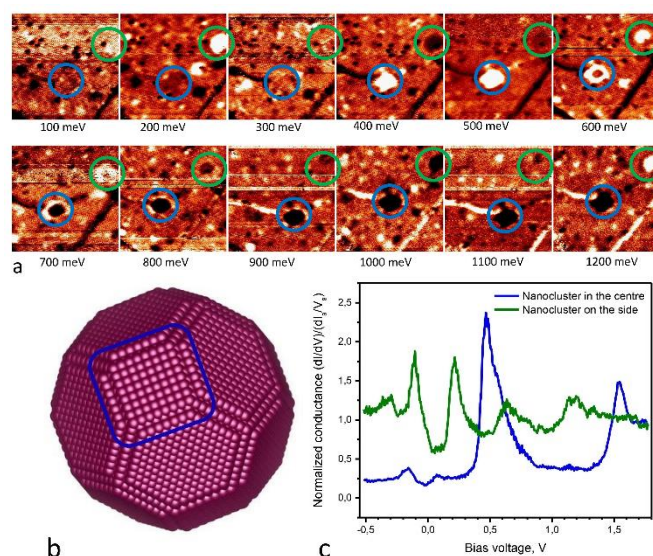


Fig. 4 (a) - Sequence of STS maps of the same area of $20 \times 20 \text{ nm}^2$ Fe(001) sample with embedded Ar nanoclusters. Periodical variation of contrast with bias appears in two large spots (encircled). The spot shape reveals some rectangular-like features; (b) - Expected shape of buried nanocluster represented by the first interface layer of Fe with the square upper (001) facet; (c) - STS normalized conductance curves showing the resonance peaks or oscillations in two spots encircled in (a).

deposited extra layers of Cu with increments of 10 nm thickness. A slight annealing to recover a flat Cu surface followed each post-deposition. The deposition was done with a calibrated effusion cell EFM3. Between each step, the sample was scanned with STM to visualise the nanoclusters.

The STM/STS measurements were done using a low-temperature STM microscope "Omicron" at temperatures of 77K and 4.7K under ultra-high vacuum. To get reliable STS measurements, we carefully conditioned the STM tips by means of local e-beam annealing. This process was controlled by checking the cold field emission from the tip. With this procedure, we were able to obtain repeatable and reliable oscillatory behaviour of the LDOS. Nevertheless, we cannot exclude some dispersion among STS spectra that could originate from the variety of the tip states at the very apex of different STM probes.

Results and discussion

Since the van der Waals binding of Ar and H atoms in the clusters is much weaker than the binding of Cu, W, or Fe atoms in the metallic crystalline lattice, the shape of the subsurface nanoclusters is determined to a great extent by the anisotropy of the surface tension of the crystal. This should provide Wulff construction [43] of the nanoclusters in the inversed form: a

hollow polyhedron with the determined facets shape. Figure 2 presents the expected shape of the last atomic layer of copper at the interface with the Ar nanocluster deduced from an estimation of the anisotropy of the Cu surface energy as well as from some experimental data [44, 45]. The atomically flat facets at the interface serve as ideal reflectors for the delocalised electron states outside the nanocluster. The nanoclusters formed in Cu crystal with the (001) and (110) cut have the same shape, however their relative orientation to the surface is different: the upper facets confining the electrons are different, therefore the electronic states used for QW formation also are different. Similarly to fcc Cu sample, the faceted nanoclusters of Ar or H are formed in bcc Fe and bcc W crystals as well, however their particular shapes differ from each other since all the crystals have different surface energies for the principal facets.

However, the shape of Co and Fe nanoclusters embedded in Cu does not follow Wulff constriction since the relatively low annealing temperature does not provide a local quasi-equilibrium state at the sample formation. Therefore, the clusters keep their flat pane cook-like shape obtained at first deposition on the surface and slight annealing. However, the roughness of the interface can be modified.

1. Fe(001) with embedded Ar nanoclusters

After preparation of the Fe(001) sample with buried Ar nanoclusters, large atomically flat terraces are observed while some steps, single defects and point-like contaminations were always presented in the STM images. STS mapping (Fig. 4) reveals these defects as black and somewhere white points of deviating conductance. However, in some locations, the surface conductance maps show also larger spots which cannot be associated with point surface additives or imperfections well recognisable also on the standard STM images. The contrast in these locations appears to be suppressed but also enhanced or unchanged depending on bias voltage and it alters periodically with the bias voltage. This is usually not the case for the objects like the surface contamination observed. Figure 4 (a) shows the series of STS maps with two such spots (encircled) periodically changing their contrast. Remarkably, the spot shape have some square feature. The STS plots (Fig4 (b)) measured in the centre of the encircled areas indeed shows the quasi-periodical variation in LDOS. The blue plot measured on the central spot (encircled blue) shows the resonances at -0.15 V, 0.5 V and 1.5 V; while the green plot corresponding to the second spot (encircled green) reveals peaks at -0.3, -0.1 V, 0.2 V, 0.65 V, and 1.2 V. All these peaks manifest the QW resonances due to electron confinement between the surface and a local interface, namely one of the facets of buried Ar nanocluster. The shape of the nanocluster is shown in Fig. 4 (c) and was calculated using surface energy of Fe according Wulff's approach. The shape of the spot obviously reflects the square-like (001) facet. The depth of location of the upper facet of the nanocluster is derived from formula 1 using the corresponding band structure of Fe [46]. The upper facet of the buried nanocluster in the centre of Figure 4 (a) (encircled blue) is located at the depth of

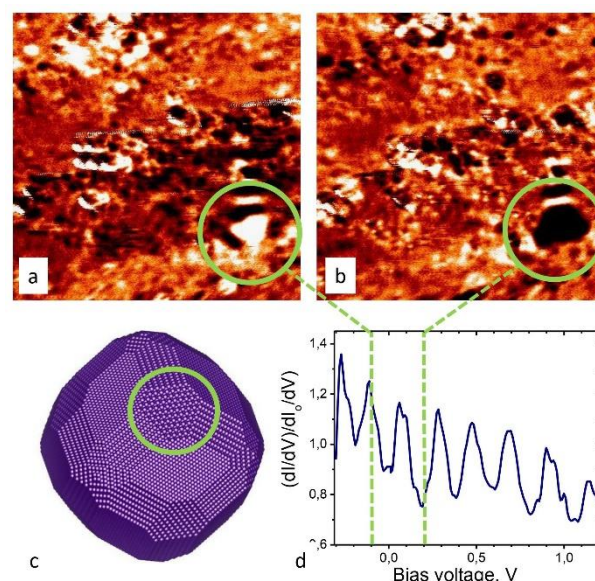


Fig. 5 (a and b) – Two STS maps $20 \times 20 \text{ nm}^2$ of the same surface of the W(111) sample with embedded H nanoclusters at bias voltage -0.1 V (a) and 0.2 V (b). The triangular feature of opposite contrast is encircled; (c) - the expected shape of H nanocluster represented by the first interface layer of W. The truncated triangular (111) facet is encircled; (d) – Plot of normalized conductance measured in the centre of the spot. The bias voltages corresponding to opposite contrast in (a) and (b) is indicated can be attributes to maximum and minimum of oscillating conductance plot.

1.3 nm below surface, whereas the corresponding facet of the second nanocluster (encircled green) is located at the depth of 2.5 nm . The distance between the resonance peaks of the shallow nanocluster is larger and the peaks themselves are stronger. The asymmetric and narrow peak shape indicates the multiple reflection of confined electrons, the condition at which the QW states are formed.

2. W(111) with embedded H nanoclusters

STS maps of the W(111) surface also show similar characteristic spots with periodically varying contrast, despite of presence of surface contamination. In the case of the (111) cut, however, the spots reveal a triangular shape and additional three ray-like features nearby with spatially varying contrast. Figure 5 (a, b) shows the STS maps of the same area, but measured at different bias voltage. Similar to the Fe(001) sample, this feature can be attributed to the upper (111) facet of having the triangular shape (Fig 5 (b)).

Measurement of normalized differential conductance or STS curve in the centre of the spot reveals the oscillations over a wide range of bias voltage. These oscillations can be associated with QW states. However, since the shape of peaks become more symmetrical and the relative amplitude is lower, we can infer a partial loss of coherence of the confined electronic states or only a few reflections in the confining region. Nevertheless,

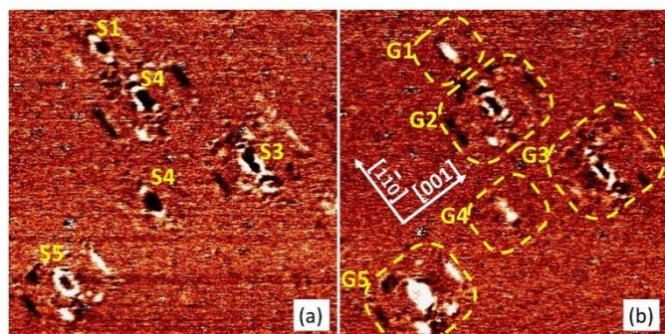


Fig. 6. Differential conductance distribution across the Cu surface (STS map), $45 \times 45 \text{ nm}^2$, at two different bias voltages: (a) 100 mV and (b) 150 mV and the tunnel current of 1.5 nA. The spots in the same positions change their contrast with bias voltage. The spots can be grouped in the uniformed ensembles of a main spot and a few satellite spots, as countered with the dashed lines. Satellite spots around some weak main spots somewhere are not well resolved.

a high contrast on the STM maps allows to determine the exact lateral location of the buried nanocluster, despite the masking image of surface contamination, while the well-resolved minima and maxima in the oscillatory curves determine the depth of reflecting nanostructure. The depth of the facet of buried nanocluster of 5.2 nm is derived from the maxima positions and the band structure of tungsten [47] using equation 1.

These two examples confirm the generalization of our approach in application to various materials. These examples also show that the amplitude of the oscillating STS signal decreases with the depth. If we proceed with deeper and deeper nano-objects, a specific depth would be reached at which the oscillations of LDOS in QW would no longer be detectable. Therefore, below we address the question about the ultimate depth of STM detection.

3. Cu(110) with embedded Ar nanoclusters: ultimate depth

As discussed above, the QW formation and capability of subsurface STM vision are determined by material characteristics such as MFP, electron coherence, surface and interface quality, and electronic states of materials used for matrix and nano-objects. In this view, the best candidate to demonstrate the ultimate depth of the subsurface STM vision would be Ar nanoclusters in the Cu(110) sample. Besides a rather long MFP in copper, which increases at low temperature, and a smooth interface with nanocluster, we also can benefit from the electron focusing effect discussed in the introduction. On the other hand, the (110) facet is the smallest one providing less efficient electron confinement between the interface and the surface. However, because of focusing in the $\langle 110 \rangle$ direction seems to be an important factor, it should compensate this disadvantage and the most intense oscillating reflected signal is expected. Therefore, with this type of sample

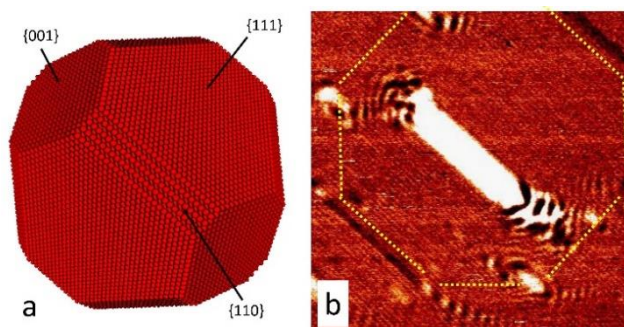


Fig. 7 (a) Expected shape of the last layer of Cu interface around Ar nanocluster; (b) High resolution STS map ($16 \times 16 \text{ nm}^2$) above an Ar nanocluster revealing the main oblong spot originated from the (110) facet, and the satellite spots corresponding to the conjunction of the {110}, {111}, and {001} facets, and the conjunction of the {111} and {001} facets. The yellow contour indicates the projected subsurface nanocluster.

we want to reach experimentally the maximal practical depth and estimate the ultimate depth that can indicate the principal capability of our approach.

After preparation, large scale STM images of the Cu(110) surface exhibit large atomically flat terraces separated by single atomic steps. The terrace surface exhibits much less contaminations. With such a clean surface, one would reasonably expect a homogenous distribution of LDOS across the terraces. However, similarly to STS maps on W(111) and Fe(001), the STS maps reveal a deviation of LDOS from its regular value in many locations. Figure 6 shows two STS maps of the same area scanned at two different biases: 100 mV (Fig. 6(a)) and 150 mV (Fig. 6(b)). The locations with deviating LDOS can be described as a system of spots of various sizes and shapes with different and variable contrasts. Some of the spots, the largest ones, are indexed with letters S1-S5 in figure 6 (a). Depending on the value of bias voltage, the spots in the same locations can be visualized on the STS maps with a lower contrast, for example the spots S1 and S5 at 100 mV (Fig. 6 (a)) or a higher contrast (see the corresponding spots at 150 mV (Fig. 6 (b))). All the spots of different shape and size are uniformly oriented and form reproducible groups encircled with dashed labelled with G1 to G5 in Fig. 6b. The groups are composed of a main oblong spot of the strongest contrast in the centre of the each group flanked by two elongated lines and surrounded by 4 more rounded small satellites spots (Fig. 6 and 7(b)). Remarkably, the oblong main spots as well as line-shaped satellite spots are all well oriented along $[1-10]$ direction. If the main spots appear with a quite low contrast, for example the spots S1 and S4, the satellite spots may be vague at some bias voltages (Fig. 6 (a)) or absent at other bias voltages (Fig. 6 (b)). The spots with oblong shape can exhibit complex differential conductance contrast. As an example, the oblong spot S5 is imaged with a white rim surrounding the dark centre (Fig. 6(a)) corresponding to enhanced and suppressed electron density, respectively. The oblong shapes of S2 and S3 show more complex features: besides a dark core and white borders, they

exhibit in addition an oscillatory contrast in the [1-10] direction also clearly seen for another object in Fig. 7b. The observed spatial oscillation of the contrast and its altering with bias voltage leads to the suggestions that these spots on the STS maps may appear due to near-surface electron scattering. It would be natural to associate each group of the ordered spots with a corresponding Ar nanocluster hidden beneath the surface [35, 36]. The top view from the (110) surface of the idealized Ar nanocluster presented with the first interface Cu layer is depicted in figure 7(a). We demonstrated previously in our work [35] the correspondence between the observed spots and specific facets: the oblong main spot has been shown to be attributed to the parallel upper (110) facet that could reflect the injected electrons back. The satellite spots are induced by the ordered atomic structure in between the {110} and {001} facets whereas the satellite lines are associated with scattering at the edges of {111} facets [35]. In other words, each observed feature can be associated with QW resonances coming from specific facets of the nanocluster. The contour line connecting the small satellite spots and passing through satellite lines gives the exact size and shape of the nanocluster

(Fig. 7(b)). As explained previously, the actual contour may appear slight asymmetrical due to deviations from the idealized shape of the nanocluster as in Fig. 7(a). However, the simple observation the spots and connecting the features on the STS maps to size and shape of hidden subsurface nanoclusters says very little about the depth of location. To obtain this parameter, we should extract the oscillating component of the LDOS versus bias voltage and apply formula 1.

Since the origin of the spots is established, the measurement of differential conductance only in the centre of main oblong spot associated with the closest (110) facet in each group is sufficient to determine the location of Ar nanocluster. The sets of these measurements for different depths is presented in figure 8. The set of measurements is performed with the sample after the deposition of each layer of copper in increments as described above. Therefore, figure 8 shows different nanoclusters selected to be of approximately equal size. By this process of fabrication and analysis we aimed at practical demonstration of ultimate depth of STM subsurface vision.

First, the differential conductance measured in the centre of main spot for all the depths (Fig. 8, see plots) clearly reveal

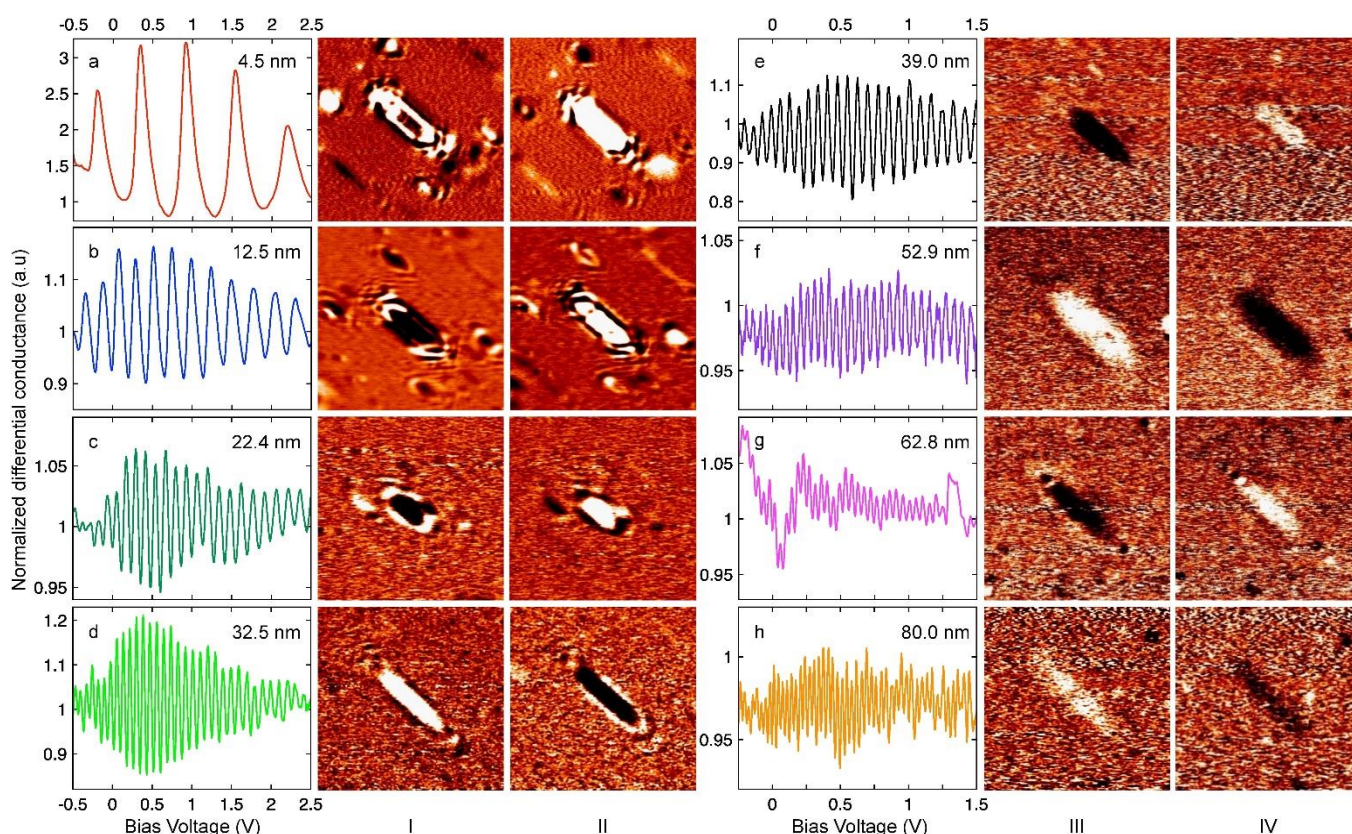


Fig. 8. Evolution of spatially resolved and normalized differential conductance as a function of burial depth: a) 4.5 nm, b) 12.5 nm, c) 22.4 nm, d) 32.5 nm, e) 39.0 nm, f) 52.9 nm, g) 62.8 nm, and h) 80.0 nm. For each specific depth (a - h), tree panels show: oscillating normalized differential conductance versus bias voltage measured in the centre of the main spot, and two maps of differential conductance (columns I, II (a-d) and columns III, IV (e-h)) recorded at two different bias voltages showing the corresponding spot with opposite contrasts. The contrast and oscillation amplitude at the depth of 80 nm (h) are high enough to detect the buried nanocluster. The shape and size of the main spot can be used to judge the size of the deep subsurface nanocluster if the satellite spots are not observed. Measurements a-d and e-h are performed at 77K and 4.5K, respectively and with different ranges of bias voltage.

remarkable oscillations versus bias voltage with the periodicities specific for each depth. This directly proves our suggestion connecting the observed spots with the subsurface scattering or QW resonances. Additionally, two STS maps with the corresponding buried nanocluster are shown on the right of each plot of oscillating normalized differential conductance in figure 8. The maps were recorded at two voltage biases corresponding to one maximum and one minimum of the differential conductance and therefore the main spots demonstrate the opposite contrasts. This also gives better understanding of the variety of contrasts for different spots observed in Fig. 6: due to the difference in the depths of location of nanocavities, the confined electronic states were in resonance or out of resonance at the chosen bias voltage. The period of oscillation determines the depth of location of the reflective facet calculated by formula 1 using tabulated data on $E(k)$ for copper [48]. The calculated depth is indicated in the upper right corner of each STS spectrum and ranges from 4.5 to 80 nm. Note that the STS spectra and maps in Fig. 8 (a – d) were obtained at 77 K, whereas those presented in Fig. 8 (e – h) were measured at 4.7 K for deeper nano-objects. The calculated depth is consistent with the estimated one by summing Ar implantation depth as described in the Experiment section which is within the typical range of 1 nm to 10 nm [49] and the resulting thickness of the copper layer added in increments of 10 nm. The satellite spots in figure 6 are well visible (a – c) at the corresponding depths of 4.5 nm, 12.5 nm and 22.4 nm, respectively, and still recognisable in the pattern (d) at the depth of 32.5 nm. The contour formed by these satellite spots and lines can reveal the size of the buried nanocluster (see similar indication in fig. 7). However, the satellite spots are no longer visible for the deeper nanoclusters, although the main spot is still observable for the depths down to 80 nm (Fig. 8 (e – h)). Their lack of visibility of the satellite spots makes impossible to estimate the size and shape of the nanoclusters buried deeper than 30 nm by the way we described above. However, the shape and size of the oblong main spot corresponding to the electron scattering from the upper (110) facet remains well visible keeping the same aspect ratio even for depths down to 80 nm (Fig. 8 (h)). Actually, this is sufficient to estimate, albeit less accurately, the size of the hidden nanocluster using an alternative assumption without using the satellite spots. If we assume the constant ratio between the size of the {110} facets and the size of other facets in the Wulff construction at the different depths, the size of the entire nanocluster can be estimated by only knowing the size of one facet. It is reasonable to assume, as the interface energy is not expected to depend on the location of nanoclusters in the bulk. Usually, near-surface relaxation, which may affect the interface tension, decays within one nanometer [50] while all our Ar nanoclusters lie much deeper. This should support our assumption.

Anyways, we have gotten a direct and impressive confirmation of subsurface STM vision really achieved for the depth of 80 nm (Fig. 8h). Since the signal-to-noise ratio is higher than 1 in both the oscillation plot and the pair of STS images, the STM is able to see even deeper.

In order to determine the ultimate depth of the STM subsurface vision, we have plotted in Fig. 9 the variation of the oscillations amplitude Q of the normalized differential conductance as a function of depth d recorded at the centre of the oblong spot. Indeed, the interpolation of such a plot would give an estimate of such ultimate depth. Data are presented in Fig. 9 for many nanoclusters of identical size to discard size dependency. The measurements were performed at two temperatures: at 77K for shallow nanoclusters and at 4.7K for deeper ones. As a consequence, the decay rate must be adjusted for these two temperatures separately. For clarity, data taken at 77K and 4.7K are indicated in red and blue, respectively in Fig. 9.

In Fig. 9, if one discard the two sets of data around a depth of 12 and 22 nm as will be discussed below, the intersection between the actual noise level drawn in green in Fig. 9 with the decay rate interpolation would lead to an ultimate depth of roughly 110 nm at 4.7 K and 70 nm at 77 K. The strong attenuation of Q for these two abovementioned sets of data could be explained by different tip termination states that could strongly alter the sensitivity to the oscillatory component of the tunnelling signal. Unfortunately, a particular electronic state at the tip apex is not always controllable and can depend on tip or can be changed over time by intentional or accidental perturbations. Therefore, the ultimate depth deduced from the plot in Fig. 9 may be underestimated and a perfect STM tip with an appropriate electronic state could provide much better results.

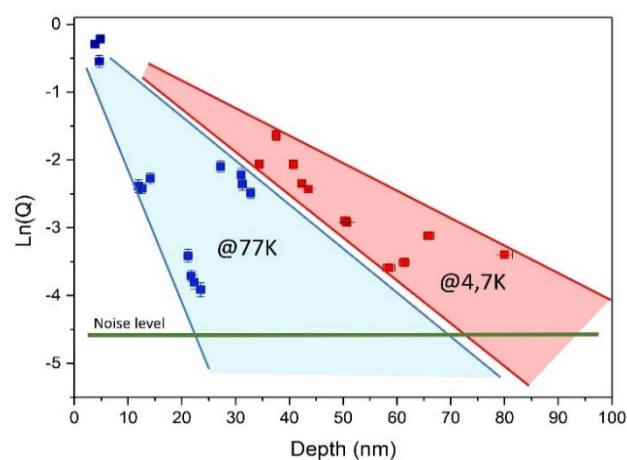


Fig.9 Amplitude of oscillatory contrast Q of the normalized conductance versus depth d measured at 77K (in blue) and 4.7K (in red). Each point corresponds to different nanocluster. Grouping the points with low oscillation amplitude in the range of 10 nm to 25 nm is due to the variation of the tip sensitivity to the oscillatory component of electronic states in some sets of measurements.

The two decay rates at two temperatures indicate that electron-phonon scattering processes influence the coherence of the electronic states. Another temperature effect usually considered when performing STS studies is the thermal broadening of the resonance states. However, in our case, it

plays an insignificant role since the periodicity in STS oscillations in our experiments is always much higher than the value of $k_B T/e$ (with k_B , Boltzmann's constant).

The reported ultimate depth could be considered as a record achievement for some exceptional case. Indeed, the favourable combination of a long MFP, a specific band structure providing the focusing effect, and total reflection from a smooth interface with the nanoclusters yields this record value for Cu(110) while other systems would provide a moderate ultimate depth. Among all the components of this combination, the role of MFP as the scaling parameter is clear, while the contribution of interface quality and focusing is not well-defined. To check the real influence of these two factors we used another systems which have more practical importance for nanomagnetism and spintronics, namely the Co and Fe nanoclusters buried in Cu(001), Cu(110) and Cu(111). The system of Co nanoclusters in Cu(001) is reported in the next sub-section, whereas similar results on Fe nanoclusters in Cu(001) are shown in Supplementary Materials. The results obtained with other orientation of copper sample are briefly discussed at the end of the following sub-section as well.

4. Cu(001) with embedded Co nanoclusters: ultimate depth without focusing

STS mapping of the flat surface reveal many locations with deviating conductance (Fig 10 (a – c)). Disregarding point defects originating from surface flaws and inclusions, relatively large spots about 5 nm are presented in the STS images. These spots are surrounded by interference rings, while the contrast of the spots depends on bias voltage. These spots are associated with the buried Co nanoclusters. The method of nanocluster forming provides the burring at the same depth. Therefore, the spots show mostly the same contrast within a chosen ensemble. However, somewhere in the ensemble the contrast can be different (Fig. 10 (b)), that implies a slightly different burring depth due to the initially stepped surface. STS measurements at the centre of a selected spot reveal oscillations in normalized surface conductance, in the same way as for the system with buried noble gas clusters. The spots on the STS maps and the oscillation in of LDOS have been registered even for deeper nanoclusters (not shown here), however at 25 nm only a very faint pattern can be observed (Fig. 10 (d)) with the corresponding oscillations of the surface conductance reduced to the noise level (Fig. 10 (h)). Therefore we can accept the ultimate depth of subsurface vision for Co nanoclusters in Cu(001) matrix as 25 nm. The same ultimate depth is obtained with Fe nanoclusters in Cu(001) (see Supplementary Materials). The measurements have been carried out at 77K. Therefore the result obtained with the non-ideal system should be compared with the result obtained with the superior system of Ar nanoclusters in Cu(110) at the same temperature, which was 70 nm. This comparison clearly shows that the partial reflection and absence of focusing reduce the ultimate depth by approximately the factor 3. Nevertheless, the ultimate depth of the subsurface vision of 25 nm for a non-ideal system is still highly impressive.

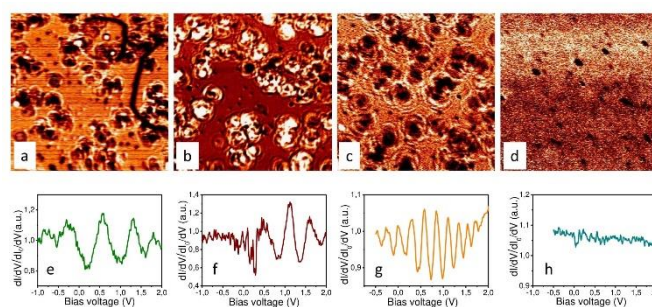


Fig. 10 (a – d) STS maps 40 x 40 nm² of Cu(001) sample with embedded Co nanoclusters buried at : (a) -3 nm, (b) -4.8 nm, (c) -10 nm, (d) -25 nm, and (e –h) the corresponding oscillatory STS plots, respectively.

Our attempts to get the subsurface STM vision of Co nanoclusters buried in Cu(111) and Cu(110) crystals did not lead to acceptable results. The first case is consistent with other observations, even using the ideal Ar nanoclusters because the Cu(111) cut does not provide the corresponding electronic states in the <111> direction. As a result, the QW states, which we want to exploit for the subsurface vision, cannot be formed in this type of sample. In contrary, the absence of QW in the system of Co nanoclusters buried in Cu(110) has another explanation. Despite the expectation of the extended ultimate depth due to the focusing effect, as for Ar nanoclusters, QWs cannot be formed assuming a rough interface. Partial intermixing at the interface which appears on the Cu(110) face more easily than on other surfaces [51, 52] should destroy the coherence at the reflection and hence the QW cannot be formed. All these observations confirm the importance of the coherence provided by the smooth interface, while the presence of focusing or partial reflection plays the secondary role in the realization of the subsurface STM vision.

5. Generalization of subsurface STM vision

The subsurface STM vision using near-surface QWs can be realised with a variety of materials as partially proven in this paper and Supplementary Materials. The generalization of our approach can also be confirmed by other practical examples of the systems where near-surface QW observations have been reported, namely Cd, Cu, Pb, Ag or Al [16-24, 29 -36], while many materials have not yet been involved in the study by this method.

The main condition of getting the subsurface vision is forming near-surface QW states. This implies a partial electron confinement of states with k -vectors in the direction perpendicular to the surface and the interface. In some cases, the appropriate electronic states of matrix material with perpendicular k -vectors may be unavailable for a particular crystalline orientation, for example as mentioned above for Cu(111), and therefore the required QW states cannot be formed. However, for a number of metals, the electronic states with perpendicular k -vectors are available in many crystalline directions. Then only the coherence requirement should be fulfilled to obtain QW states. This means that the width of

confinement, which is in fact equal to the depth of subsurface vision, should be smaller than the coherence length. The latter is generally limited by MFP and ranges from a few nanometers to several tens of nanometers, depending on the type of metals, their purity and temperature. Since MFP depends on temperature, cooling down should increase the depth of subsurface STM vision. The condition for the partial confinement is also not very strict: the interface with conducting nano-objects provides sufficient reflection to form the near-surface QW.

However, a rough interface at the combination of two materials can completely destroy the coherence of reflected electron waves. The rough interface can be formed at some specific crystalline orientations or due to the intermixing of two materials. Focusing, on the other hand, is not as crucial for achieving the subsurface STM vision, although this effect can increase the ultimate detection depth and enhance the resolution.

Since the crucial parameters of all other systems do not exceed the excellent parameters of the system of Ar nanoclusters in Cu(110), we can consider that we have found the real limit for the subsurface STM vision. Nevertheless, even if the depth of subsurface characterization with other type of materials would be several times less than 100 nm, we can still claim the QW-assisted subsurface STM vision as a promising method for many applications.

Conclusions

We have presented the concept and the experimental proof of deep subsurface vision using STM. Nano-objects hidden below the surface can be characterised by STM if they are buried in the range of several nanometers up to 110 nm deep. In that sense, it brings bulk sensitivity available to STM which is a method commonly known to for surface characterization. Our approach is based on the use of near-surface QW states formed in the host material due to the electron confinement between the surface and buried nano-objects. These QW states, probed on the surface by STS, reveal periodic oscillation of LDOS. The spatial variation of oscillatory LDOS carries information about location, size, and, in some cases, shape of buried nano-objects while the oscillation period of LDOS defined by the QW width, determines the depth of hidden nano-object. The effect of electron focusing due to a specific band structure of the host material enhances the ultimate depth of the STM subsurface vision. These results put in evidence that the STM is well suitable for non-destructive 3D characterisation near the surface. Our approach can be applied to various combination of materials.

Author Contributions

O. K. and M. S. contributed equally to this work. O.K. carried out the low-temperature-STM/STS experiments and treated the results. O.K. and M.S. initially wrote the manuscript and all the authors contributed. E.G. performed the theoretical

calculations of band structure and Wulff constructions. O. K. did the sample fabrication at the assistance of D. P.; Y. L. fabricated Fe samples and helped at interpretation of QW results. S.M. and O.K. supervised the work. All authors approved the final version of the manuscript.

Conflicts of interest

There are no conflicts to declare.

Acknowledgements

This work was supported by the French PIA project “Lorraine Université d’Excellence” reference ANR-15-IDEX-04-LUE, and by the project CAP-MAT supported by the “FEDER-FSE Lorraine et Massif Vosges 2014–2020”, a European Union Program. O.K. was supported by the region Grand Est under the DESOMIN project. O.K. and S.M. acknowledge the financial support of the Institut Carnot ICEEL. We are thankful to Can Avci and Bert Koopmans for their interest at preliminary results, and to Mattijn Cox for offering a graphical illustration for figure 1. We also want to recollect the memory of Karl-Heinz Rieder (1942 – 2017) who appreciated our very first results in private communications and inspired us for going further. Computing resources were provided by the EXPLOR centre hosted by the University de Lorraine.

References

- 1 G. Binning, H. Rohrer, Ch. Gerber, and E. Weibel, *Phys. Rev. Lett.*, 1982, **49**, 57.
- 2 R. Wiesendanger, *Scanning Probe Microscopy and Spectroscopy: Methods and Applications*, Cambridge, UK: Cambridge University Press, 1994.
- 3 T. Takigami and M. Tanimoto, *Appl. Phys. Lett.*, 1991, **58**, 2288.
- 4 R.S.R. Gajjala, A.L. Hendriks, A. Alzeidan, T.F. Cantalice, A.A. Quivy, and P. M. Koenraad, *Phys. Rev. Mat.*, 2020, **4**, 114601.
- 5 J. Mayer, L.A. Giannuzzi, T. Kamino, and J. Michael, *MRS Bulletin*, 2007, **32**, 400.
- 6 R. Busch, C. Tieleman, S. Reinsch, R. Müller, C. Patzig, M. Krause, and T. Höche, *Micron*, 2021, **150**, 103090.
- 7 Y. Lu, D. Li, and F. Liu, *Materials*, 2022, **15**, 307.
- 8 J. Osing and I.V. Shvets, *Surf. Sci.*, 1998, **417**, 145.
- 9 T. Siahann, O. Kurnosikov, H. J. M. Swagten, and B. Koopmans, *Phys. Rev. B*, 2014, **90**, 165419.
- 10 A. Rai, J. Nayak, S.R. Barman, *Appl. Surf. Sci.*, 2015, **332**, 260.
- 11 J. K. Garleff, A. P. Wijnheijmer, and P. M. Koenraad, *Semicond. Sci. Technol.*, 2011, **26**, 064001.
- 12 J.-M. Jancu, J.-Ch. Girard, M.O. Nestoklon, A. Lemaître, F. Glas, Z.Z. Wang, and P. Voisin, *Phys. Rev. Lett.*, 2008, **101**, 196801.
- 13 A.P. Wijnheijmer, J.K. Garleff, K. Teichmann, M. Wenderoth, S. Loth, R.G. Ulbrich, P.A. Maksym, M. Roy, and P.M. Koenraad, *Phys. Rev. Lett.*, 2009, **102**, 166101.
- 14 G. Mahieu, B. Grandidier, D. Deresmes, J.P. Nys, D. Stiévenard, and Ph. Ebert, *Phys. Rev. Lett.*, 2005, **94**, 026407.
- 15 M. Roy and P.A. Maksym, *J. Physics.*, 2014, **526**, 012008.
- 16 I. B. Altfeder, K. A. Matveev, and D. M. Chen, *Phys. Rev. Lett.*, 1997, **78**, 2815.

- 17 J. Kim, S. Qin, W. Yao, Q. Niu, M. Y. Chou, and C.-K. Shih, *Proceed. Nat. Acad. Sci. (PNAS)*, 2010, **107**, 12761.
- 18 J. Kim, S. Qin, Y. Zhang, W. Zhu, and C.-K. Shih, *Surf. Sci.*, 2015, **632**, 174.
- 19 R. Otero, A.L. Vazquez de Parga, and R. Miranda, *Surf. Sci.*, 2000, **447**, 143.
- 20 C. Liu, C. Zhao, S. Zhong, C. Chen, Z. Zhang, Y. Jia, and J. Wang, *Nano Lett.*, 2021, **21**, 9285.
- 21 J.-F. Jia, S.-C. Li, Y.-F. Zhang, and Q.-K. Xue, *J. Phys. Soc. Jap.*, 2007, **76**, 082001.
- 22 M. Müller, N. Néel, S. Crampin, and J. Köger, *Phys. Rev. Lett.*, 2016, **117**, 136803.
- 23 M. Müller, N. Néel, S. Crampin, and J. Köger, *Phys. Rev. B*, 2017, **96**, 205426.
- 24 M.-L. Tao, H.-F. Xiao, K. Sun, Y.-B. Tu, H.-K. Yuan, Z.-H. Xiong, J.-Z. Wang, and Q.-K. Xue, *Phys. Rev. B*, 2017, **96**, 125410.
- 25 A. Weismann, M. Wenderoth, S. Lounis, P. Zahn, N. Quaas, R.G. Ulbrich, P.H. Dederichs, and S. Blügel, *Science*, 2009, **323**, 1190.
- 26 T. Kotzott, M. Bouhassoune, H. Prüser, A. Weismann, S. Lounis, and M. Wenderoth, *New J. Phys.*, 2021, **23**, 113044.
- 27 Ye. S. Avotina, Yu. A. Kolesnichenko, and J. M. van Ruitenbeek, *Low Temperature Phys.*, 2010, **36**, 849.
- 28 S. Lounis, P. Zahn, A. Weismann, M. Wenderoth, R.G. Ulbrich, I. Mertig, P.H. Dederichs, and S. Blügel, *Phys. Rev. B*, 2011, **83**, 035427.
- 29 M. Schmid, W. Hebenstreit, P. Varga, and S. Crampin, *Phys. Rev. Lett.*, 1996, **76**, 2298.
- 30 M. Schmid, S. Crampin, and P. Varga, *J. Electron. Spectrosc. Relat. Phenom.*, 2000, **109**, 71.
- 31 C. Sproadowski and K. Morgenstern, *Phys. Rev. B*, 2010, **82**, 165444.
- 32 M. Ruby, B. W. Heinrich, J. I. Pascual, and K. J. Franke *Phys. Rev. Lett.*, 2015, **114**, 157001.
- 33 O. Kurnosikov, O.A.O. Adam, H.J.M. Swagten, W.J.M. de Jonge, and B. Koopmans, *Phys. Rev. B*, 2008, **77**, 125429.
- 34 O. Kurnosikov, J.H. Nietsch, M. Sicot, H.J.M. Swagten, and B. Koopmans, *Phys. Rev. Lett.*, 2009, **102**, 066101.
- 35 O. Kurnosikov, H.J.M. Swagten, and B. Koopmans, *Phys. Rev. Lett.*, 2011, **106**, 196803.
- 36 O. Kurnosikov, D.V. Kulikov, V.S. Kharlamov, H.J.M. Swagten, and Y.V. Trushin, *Phys. Rev. B*, 2011, **84**, 054109.
- 37 L. Burgi, H. Brune, O. Jeandupeux, and K. Kern *J. Electron. Spectrosc. Relat. Phenom.*, 2000, **109**, 33.
- 38 S. Ogawa, H. Nagano, and H. Petek, *Phys. Rev. B*, 1997, **55**, 10869.
- 39 H.T. Nguyen-Truong, *Appl. Phys. Lett.*, 2016, **108**, 172901.
- 40 U. Mizutani, *Introduction to the electron theory of metals* (Cambridge University Press, New York, 2001), 1st ed.
- 41 P.L. de Andres, F.J. Garcia-Vidal, K. Reuter, F. Flores, *Progr. Surf. Sci.*, 2001, **66**, 3.
- 42 K. Reuter, P.L. de Andres, F. J. Garcia-Vidal, F. Flores, and K. Heinz, *Phys. Rev. B*, 2001, **63**, 205325.
- 43 R. Tran, Z. Xu, B. Radhakrishnan, D. Winston, W. Sun, K.A. Persson, and S.P. Ong, *Sci. Data*, 2016, **3**, 16008.
- 44 K.-T. Chen, W.-Ch. Chang, S.-Ch. Lu, Po-Yu. Yang, and H.-Yu Tuan, *J. Nanomaterials*, 2019, **2019**, 2890162.
- 45 Zh. Ren, N. Liu, B. Chen, J. Li, and D. Mei, *J. Phys. Chem. C* 2018, **122**, 27402.
- 46 J. Appl. Phys. 105, 093709 (2009)
- 47 L. F. Mattheiss, *Phys. Rev.* 139, 1893 (1965)
- 48 G.A. Burdick, *Phys. Rev.*, 1963, **129**, 138.
- 49 J. S. Pan, A. T. S. Wee, C. H. A. Huan, H. S. Tan, and K. L. Tan, *J. Appl. Phys.*, 1996, **79**, 2934.
- 50 P.M. Marcus, X. Qian, and W. Hübner, *J. Phys. Condens. Matter*, 2000, **12**, 5541.
- 51 O.V. Stepanyuk, N.N. Negulyaev, A.M. Saletsky, and W. Hergert, *Phys. Rev. B*, 2008, **78**, 113406.
- 52 H. Wen, M. Neurock, and H.N.G. Wadley, *Phys. Rev. B*, 2007, **75**, 085403.